SISSA

PAPER

Impact of COHERENT measurements, cross section uncertainties and new interactions on the neutrino floor

To cite this article: D. Aristizabal Sierra *et al* JCAP01(2022)055

View the article online for updates and enhancements.

Impact of COHERENT measurements, cross section uncertainties and new interactions on the neutrino floor

D. Aristizabal Sierra,[a] **V. De Romeri,**[b] **L.J. Flores**[c,d] **and D.K. Papoulias**[e]

[a]Universidad Técnica Federico Santa María - Departamento de Física
  Casilla 110-V, Avda. España 1680, Valparaíso, Chile
[b]Instituto de Física Corpuscular, CSIC/Universitat de València,
  Calle Catedrático José Beltrán, 2 E–46980 Paterna, Spain
[c]Instituto de Física, Universidad Nacional Autónoma de México,
  A.P. 20–364, Ciudad de México 01000, México
[d]Tecnológico Nacional de México/ITS de Jerez,
  C.P. 99863, Zacatecas, México.
[e]Department of Physics, University of Ioannina,
  GR–45110 Ioannina, Greece
  E-mail: daristizabal@ulg.ac.be, deromeri@ific.uv.es, ljflores@jerez.tecnm.mx,
  d.papoulias@uoi.gr

Abstract. We reconsider the discovery limit of multi-ton direct detection dark matter experiments in the light of recent measurements of the coherent elastic neutrino-nucleus scattering process. Assuming the cross section to be a parameter entirely determined by data, rather than using its Standard Model prediction, we use the COHERENT CsI and LAr data sets to determine WIMP discovery limits. Being based on a data-driven approach, the results are thus free from theoretical assumptions and fall within the WIMP mass regions where XENONnT and DARWIN have best expected sensitivities. We further determine the impact of subleading nuclear form factor and weak mixing angle uncertainties effects on WIMP discovery limits. We point out that these effects, albeit small, should be taken into account. Moreover, to quantify the impact of new physics effects in the neutrino background, we revisit WIMP discovery limits assuming light vector and scalar mediators as well as neutrino magnetic moments/transitions. We stress that the presence of new interactions in the neutrino sector, in general, tend to worsen the WIMP discovery limit.

Contents

1 Introduction

Cosmological and astrophysical data support the idea that dark matter (DM) is the dominant form of matter in the Universe. One of the most considered hypothesis is that of DM being a thermal species weakly coupled to the thermal bath and whose abundance is determined by thermal freeze-out (a species usually referred to as WIMP). The main motivation for such a scenario is — arguably — the fact that its abundance is entirely determined by the Universe expansion rate and by the interactions of the DM particle with the early Universe thermal bath. This means that once a cosmological and a particle physics model are specified, the determination of the DM abundance is to a large extent reduced to a parameter space-related question. A rather large list of such models exist and have been the subject of a great deal of phenomenological and experimental activity, which includes — among others — the direct detection of DM in laboratory experiments.

The DM direct detection program dates back to the early nineties, with the first germanium ionization detectors using few kilogram target material [1]. The most up-to-date data, which lead to the most stringent limits on the DM-nucleon cross section, follow from measurements of order ton-size liquid xenon (LXe) time projection chambers (TPCs) and include the LUX, PandaX-II and XENON1T experiments [2–4]. Measurements on liquid argon (LAr) TPCs, which include DarkSide-50 and DEAP-3600, have as well placed limits, albeit less stringent due to their lower exposures and higher recoil energy thresholds [5, 6]. In the next few years searches will continue, with LXe TPC experiments paving the way. Future experiments include LZ, XENONnT and ultimately DARWIN, detectors which involve multi-ton fiducial volumes [7–10]. The advent of the multi-ton era implies that DM searches will be subject to irreducible neutrino backgrounds, in particular those emitted in the ^{8}B process of the solar pp chain [11, 12].

Neutrino backgrounds induce coherent elastic-neutrino nucleus scattering (CEνNS) and so produce nuclear recoil spectra, which, depending on the WIMP parameter space, can

have a strong degeneracy with those expected from spin-independent WIMP interactions.[1] Actually, a full degeneracy is found between ^{8}B solar (atmospheric) neutrinos and a WIMP model defined by a WIMP mass $m_\chi \simeq 6\,\mathrm{GeV}$ and a WIMP-nucleon cross section $\sigma_{n-\chi} \simeq 5 \times 10^{-45}\,\mathrm{cm}^2$ ($m_\chi \simeq 100\,\mathrm{GeV}$ and $\sigma_{n-\chi} \simeq 10^{-48}\,\mathrm{cm}^2$) [12]. This level of degeneracy thus leads to a saturation of the WIMP-nucleon cross section to which a particular experiment can have access. So, in contrast to the background-free paradigm, increasing exposure does not imply a linear improvement of sensitivities but rather a saturation of its discovery limit [11], typically referred to as *neutrino floor*. Various experimental techniques that enable overcoming the neutrino floor have been discussed in the literature. They include measurements of the WIMP and neutrino recoil spectra tails [14], directionality (see e.g. [15]), measurements with different material targets [14] and annual modulation [16]. However, although feasible in principle, some of them require large exposures and/or further technological improvements.

The experimental reach of multi-ton DM direct detection experiments (with no directional capabilities) thus depends crucially on the precision with which WIMP and CEνNS induced events can be predicted. WIMP event rates are subject to astrophysical uncertainties, which depend e.g. on the DM halo model assumed for their calculation. Their impact have been studied in detail in ref. [17]. CEνNS event rate uncertainties instead can be thought as being of two types, those associated with neutrino flux normalizations and those associated with the CEνNS cross section. The Standard Model (SM) CEνNS cross section uncertainties are mainly driven by nuclear physics effects, encoded in the weak-charge form factor [18–20]. For solar neutrinos these effects barely exceed $\sim 1\%$, while for atmospheric neutrinos they can be larger but never exceeding $\sim 10\%$. For this reason, the neutrino flux normalization uncertainties dominate the determination of the experimental reach a given experiment can have.

The advent of the multi-ton era requires an understanding of the discovery reach beyond that implied by the neutrino flux normalization factors uncertainties. Since the effects of astrophysical uncertainties have been already quantified, and have been proved to have a small effect [17], for this task one should rather focus on the uncertainties in the neutrino sector. In order to do so one can adopt a data-driven approach or instead consider all possible effects that might have an impact on the discovery potential. This paper aims at exploring both cases for LXe and LAr detectors. With *data-driven* analysis we mean using COHERENT data [21–23] to extract the CEνNS cross section along with its uncertainty. The advantage of this approach is that in such a way the cross section uncertainty encapsulates all possible effects, including possible new physics contributions, without the need of any further assumption. We present as well a more assumption-dependent analysis in which we consider what could be regarded as sub-leading uncertainties. These include effects related with possible low-energy variations of the weak mixing angle and the unknown value of the xenon point-neutron distribution mean-square radius. Finally, given the precision with which CEνNS has been currently measured, possible new physics effects can have a big impact too (see for instance [24–30]). Here, we present an analysis of such effects by considering new vector and scalar interactions in the light regime as well as neutrino magnetic moments/transitions.

The remainder of this paper is organized as follows. In section 2 we discuss WIMP and event rate spectra along with the likelihood method that we use for the determination of discovery limits. In section 3 we present the results of our analyses obtained following the data-driven approach and considering sub-leading uncertainty effects and new interactions.

---

[1]Certain spin dependent or spin and velocity dependent WIMP interactions can also induce recoil spectra that degenerate with the neutrino recoil spectra [13].

In section 4 we present our conclusions. Finally, in appendix A we provide details of the procedure used for the extraction of the CEνNS cross section from COHERENT data.

2 WIMP and neutrino event rates

In this section we present a brief discussion of the event rates induced by the interactions of the DM particles (in the local DM halo) and neutrinos with the nuclear target material of a generic detector. On dimensional grounds, event rates can be estimated to be given by the number of scatterers N_N, the incident particle flux Φ and the interaction probability of the incident particles with the scatterers σ. In terms of these variables, the number of expected events per unit of amount of target material and per time is given by $R \sim N_N \times \Phi \times \sigma$. For DM, astrophysical assumptions on the DM halo model are required to predict the WIMP flux at the detector. As for neutrinos, fluxes fall in three categories: solar, diffuse supernova neutrino background (DSNB) and sub-GeV atmospheric neutrinos. Whether a certain type or component matters or not for a certain detector depends on the energy threshold. In particular, for LXe detectors it is known that only the ^{8}B component of the solar neutrino spectrum matters [12, 14]. Here however we consider all components, which allows to extend our analysis to a wider DM mass range.

Discussion of solar, DSNB and sub-GeV atmospheric neutrino fluxes have been presented in a wide spectrum of references. As backgrounds for DM direct detection searches they have been discussed in detail in refs. [11, 12, 17, 26, 31–34]. Some of their main properties can be found also in standard textbooks (see e.g. [35]). Briefly, solar neutrinos are generated in certain sub-processes of the pp chain cycle which accounts for the hydrogen-helium fusion process responsible for most of the solar energy. They are produced as well in the carbon-nitrogen-oxygen (CNO) cycle, which for a main sequence star accounts for less then $\sim 2\%$ of its energy. The neutrino spectrum from the pp chain involves three monochromatic lines at $E_\nu = 0.38\,\mathrm{MeV}$ ($^7\mathrm{Be} + e^- \rightarrow \nu_e + ^7\mathrm{Li}^*$), $E_\nu = 0.86\,\mathrm{MeV}$ ($^7\mathrm{Be} + e^- \rightarrow \nu_e + ^7\mathrm{Li}$) and $E_\nu = 1.4\,\mathrm{MeV}$ (pep), along with three continuous spectra (pp, ^{8}B and hep) which extend up to energies of order $16\,\mathrm{MeV}$ (hep). The CNO cycle involves instead three continuous spectra (^{13}N, ^{15}O, ^{17}F) whose kinematic tails are located at $\sim 1.2\,\mathrm{MeV}$.

The DSNB stems from the cumulative flux of neutrinos from supernova (SN) explosions all over the history of the Universe. Compared to solar neutrino fluxes it is less abundant but it matters once the hep neutrino flux reaches its kinematic tail. Since DSNB neutrino energies are determined by SN dynamics, the flux extends only up to $E_\nu \sim 50\,\mathrm{MeV}$. At $E_\nu \sim 30\,\mathrm{MeV}$ however, the sub-GeV atmospheric neutrino flux kicks in and dominates the neutrino spectrum up to the energies that matter for CEνNS, $\sim 200-300\,\mathrm{MeV}$. Atmospheric neutrinos arise from cosmic rays interactions with the Earth atmosphere and the subsequent decays of pions and muons.

For solar neutrinos, predictions from the B16-GS98 high-metallicity standard solar model (SSM) [36] are used. For DSNB neutrino fluxes we instead use values that follow from theoretical predictions relying on the assumption that the SN neutrino spectrum is well approximated by a Fermi distribution with temperatures in the 3-8 MeV range [11, 37]. For sub-GeV atmospheric neutrinos we use the predictions obtained in ref. [38] from Monte Carlo simulations of cosmic-ray cascades. Note that in contrast to WIMP fluxes as well as DSNB and sub-GeV atmospheric neutrino fluxes, almost all solar neutrino flux components have been measured, with neutrinos from the ^{15}O CNO cycle subprocess being the most recent measurement [39–42]. Since DM direct detection experiments rely on nuclear recoil mea-

Neutrino flux components normalizations and uncertainties					
Comp.	Norm. [$\text{cm}^{-2} \cdot \text{s}^{-1}$]	Unc.	Comp.	Norm. [$\text{cm}^{-2} \cdot \text{s}^{-1}$]	Unc.
^7Be (0.38 MeV)	4.84×10^8	3%	^7Be (0.86 MeV)	4.35×10^9	3%
pep	1.44×10^8	1%	pp	5.98×10^{10}	0.6%
^8B	5.25×10^6	4%	hep	7.98×10^3	30%
^{13}N	2.78×10^8	15%	^{15}O	2.05×10^8	17%
^{17}F	5.29×10^6	20%	DSNB	86	50%
Atm	10.5	20%	—	—	—

Table 1. Neutrino flux normalization factors along with their uncertainties as predicted by the B16-GS98 high metallicity SSM [36]. Values follow the recommendations pointed out in ref. [47]. These values along with those in table 2 are used in the determination of WIMP discovery limits.

surements, solar neutrino events are dominated by the ^8B neutrino flux. Measurements of this flux have been performed at Super-Kamiokande (SK) and BOREXINO using neutrino-electron elastic scattering events and at SNO using neutrino scattering on deuteron [43–45]. Exposures at BOREXINO are of the order of 300 tonne-year, while at SK and SNO above 1000 tonne-year. These numbers imply that DM detectors could provide complementary information on the ^8B neutrino flux (nuclear channel instead of electron channel), but will not have the capability to improve upon the uncertainties these experiments have placed. In contrast, in the atmospheric sector they can provide the first ever measurement of sub-GeV neutrino fluxes. This will require exposures of the order of 700 tonne-year, but provided they can be achieved this will lead to a 5σ observation [46]. Direct measurement of the atmospheric component will certainly reduce current uncertainties, entirely determined by Monte Carlo simulations. Neutrino flux normalization factors along with their uncertainties are displayed in table 1.

The CEνNS differential recoil spectrum follows from a convolution of neutrino fluxes and the CEνNS differential cross section. For the α-th flux component it reads

$$\frac{dR_\nu}{dE_r} = \varepsilon \frac{N_A}{m_{\text{target}}} \int_{E_\nu^{\min}}^{E_\nu^{\max}} \frac{d\Phi_\alpha}{dE_\nu} \frac{d\sigma}{dE_r} dE_\nu \; . \tag{2.1}$$

Here ε refers to the exposure in ton·year units, N_A to the Avogadro number in mol^{-1} units, m_{target} to the nuclear target molar mass and $d\Phi_\alpha/dE_\nu$ to the neutrino flux (including its normalization). The integration lower limit is determined by the recoil energy according to $E_\nu^{\min} = \sqrt{m_N E_r/2}$, with m_N the scatterers' nuclear mass. Since xenon has 9 stable isotopes, of which few of them have substantially large natural abundances, in our analyses we work with averaged nuclear mass and mass number: $m_N = \sum_i m_i X_i$ and $A = \sum_i A_i X_i$, with the sum running over all stable isotopes. The integration upper limit is determined by the flux kinematic tail. The total number of CEνNS events induced by the α-th flux is thus given by

$$N_\nu(\Phi_\alpha) = \int_{E_r^{\min}}^{E_r^{\max}} \frac{dR_\nu}{dE_r} dE_r \tag{2.2}$$

where $E_r^{\min}$ refers to recoil energy threshold and $E_r^{\max} \simeq 2E_\nu^2|_{\text{tail}}/m_N$.

Relevant WIMP related parameters			
v_0 [km/s]	v_{lab} [km/s]	v_{esc} [km/s]	ρ_0 [GeV/cm^3]
220	232	544	0.3

Table 2. Values for the average, laboratory and escape velocities along with the local halo DM density $\rho_0 = \rho(R_0 = 8\,\mathrm{kpc})$ used in the determination of WIMP discovery limits.

The CEνNS differential scattering cross section, determined by a neutral current process, is given by [48, 49]

$$\frac{d\sigma}{dE_r} = \frac{m_N G_F}{2\pi} Q_W^2 F_W^2(q) \left(2 - \frac{m_N E_r}{E_\nu^2} \right) , \tag{2.3}$$

where Q_W is the coherent weak charge that quantifies the coupling of the Z gauge boson to the nucleus. It is therefore entirely determined by electroweak $Z - q$ couplings, namely

$$Q_W = (A - Z)(g_V^u + 2g_V^d) + Z(2g_V^u + g_V^d) , \tag{2.4}$$

with the couplings given by $g_V^u = 1/2 - 4/3 \sin^2 \theta_W$ and $g_V^d = -1/2 + 2/3 \sin^2 \theta_W$. For the weak mixing angle, in our analyses, we use its low-energy value obtained by the RGE extrapolation from the Z scale to $q^2 = 0$, $\sin^2 \theta_W = 0.2387$ [50]. The cross section in eq. (2.3) comes along with the weak-charge nuclear form factor which, combined with the coherent weak charge, determines the q-dependent strength of the Z-nucleus coupling. Throughout the paper we use the Helm parametrization [51]. For the impact of uncertainties due to the variations of the point-neutron distribution mean-square-radius (R_n), however, we express the weak-charge form factor in terms of the spin-independent proton and neutron form factors (for which, again, we use the Helm parametrization), neglecting nucleon form factor q-dependent terms (more details are given in section 3.1.2). Note that choosing a particular form factor parametrization implies that our results involve, depending on the momentum transfer, up to a $\sim 10\%$ theoretical uncertainty for both the WIMP and CEνNS event rates [52, 53].

On the other hand, the WIMP differential recoil spectrum can be written according to

$$\frac{dR_W}{dE_r} = \varepsilon \frac{\rho_0 \sigma_{\mathrm{SI}}(q)}{2m_\chi \mu^2} \int_{|\boldsymbol{v}|>v_{\min}} d^3 v \, \frac{f(\boldsymbol{v})}{v} , \tag{2.5}$$

where $\rho_0 = \rho(R_0)$ ($R_0 = 8\,\mathrm{kpc}$) is the local halo DM density, $\sigma_{\mathrm{SI}}(q)$ is the spin-independent momentum-transfer-dependent WIMP-nucleus scattering cross section, m_χ is the WIMP mass and μ is the WIMP-nucleus reduced mass: $\mu = m_\chi m_N/(m_\chi + m_N)$. The integral corresponds to the mean inverse speed and its value is determined by the assumed velocity distribution. The minimum WIMP velocity, $v_{\min}$, that can induce a nuclear recoil with energy E_r depends on whether the scattering is elastic ($\chi + N \to \chi + N$) or inelastic ($\chi + N \to \chi' + N$). For elastic scattering, for which our results apply,[2] one finds $v_{\min} = \sqrt{m_N E_r/2}/\mu$. As for illustration, we show in figure 1 the neutrino and WIMP differential recoil spectra expected in the SM (left panel) and in a new physics scenario with a light vector mediator (right panel), which we will discuss in more detail in section 3.2. The WIMP mass has been fixed to 6 GeV and the WIMP-nucleon momentum-transfer-independent cross section has been taken along

---

[2]Inelastic contributions to the event rate are suppressed [54].
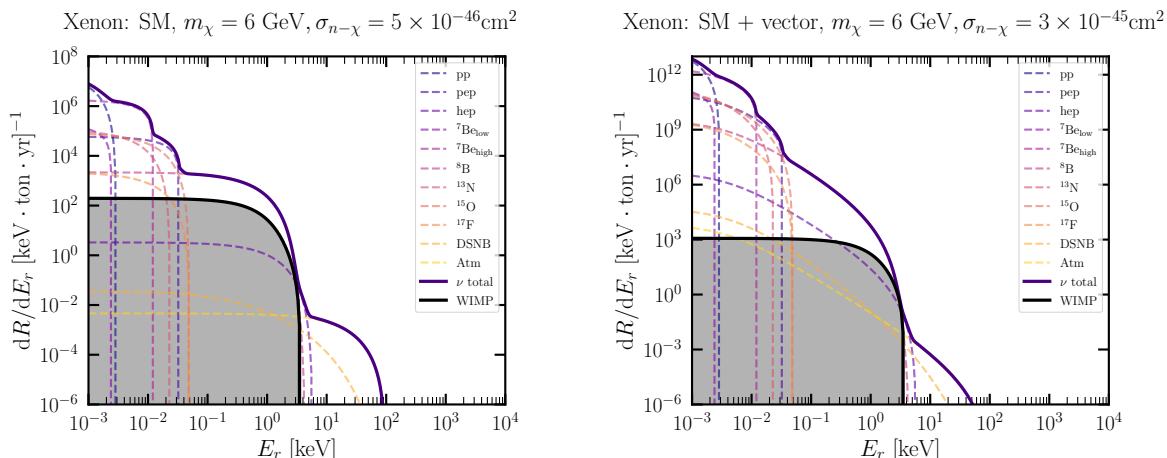
Figure 1. *Left graph*: neutrino and WIMP differential recoil spectra expected in the SM. *Right graph*: neutrino and WIMP differential recoil spectra in the presence of a long-range vector interaction.

the corresponding WIMP discovery limit shown in figure 5 (left), obtained assuming a xenon detector with an exposure of 1 ton·yr. This choice of WIMP mass and cross section leads to a WIMP differential rate which mimics almost exactly the differential rate of ^{8}B solar neutrinos.

The total number of WIMP events is obtained by integrating eq. (2.5)

$$N_W = \int_{E_r^{\min}}^{E_{\max}} \frac{dR_W}{dE_r} dE_r \,, \tag{2.6}$$

where $E_{\max} = 2\mu^2(v_{\rm esc} + v_{\rm lab})^2/m_N$ (see discussion below) [55].

In scenarios where the WIMP-proton and WIMP-neutron scattering cross sections are equal (spin-conserving scenarios, $f_p/f_n = 1$), and nucleon form factor q-dependent terms are neglected, $\sigma_{\rm SI}(q)$ can be written as

$$\sigma_{\rm SI}(q) = \frac{\mu^2}{\mu_n^2} \left[ZF_p(q) + (A - Z)F_n(q) \right]^2 \sigma_{\chi-n} \,, \tag{2.7}$$

where $\sigma_{\chi-n}$ is the WIMP-nucleon momentum-transfer-independent cross section and μ_n refers to the WIMP-nucleon reduced mass, $\mu_n = m_\chi m_n/(m_\chi + m_n)$ with $m_n = 931.5$ MeV. This expression is particularly useful in the treatment of uncertainties related with the point-neutron distribution mean-square-radius. Here $F_{n,p}(q)$ are spin-independent neutron and proton nuclear form factors which, as in the neutrino sector, we parametrize à la Helm. Of course if one assumes the point-nucleon distribution mean-square-radii to be equal a much more simple (and familiar) relation follows

$$\sigma_{\rm SI}(q) = \frac{\mu^2}{\mu_n^2} A^2 \sigma_{n-\chi} F^2(q^2) \,. \tag{2.8}$$

In all our analyses, apart from that related with form factor uncertainties, we make this simplifying assumption (see section 3.1.2 for further details).

The results presented in the following sections are obtained assuming the standard halo model (SHM) [56, 57], which assumes that the local DM halo is dominated by a

smooth and virialized component (non-virialized components, such as streams or debris flows, are regarded as subleading), well described by an isothermal sphere with an isotropic and Maxwellian velocity distribution according to

$$f(v) = \begin{cases} \frac{1}{N_{\rm esc}} \left(\frac{3}{2\pi\sigma_v^2} \right)^{3/2} e^{-3v^2/2\sigma_v^2} & \text{for} \quad v < v_{\rm esc}\,, \\ 0 & \text{for} \quad v > v_{\rm esc}\,, \end{cases} \quad . \tag{2.9}$$

where σ_v refers to the root-mean-square velocity dispersion which determines the average (most likely) speed $v_0 = \sqrt{2/3}\sigma_v$. The normalization factor is in turn given by

$$N_{\rm esc} = \text{erf}\left(\frac{v_{\rm esc}}{v_0} \right) - \frac{2}{\sqrt{\pi}} \frac{v_{\rm esc}}{v_0} e^{-v_{\rm esc}^2/v_0^2}\,. \tag{2.10}$$

The Maxwellian distribution is truncated at the escape velocity, $v_{\rm esc}$, to account for the fact that for larger values the DM is not any more gravitationally bounded and thus can escape the Galaxy gravitational pull. With $f(v)$ defined as in eq. (2.9), and after a Galilean boost to the laboratory (Earth) frame (with velocity $v_{\rm lab}$), the mean inverse speed can be analytically calculated. Being a standard well-known result it can be found in many references. We point the reader to e.g. ref. [58]. Values for the relevant parameters used in our calculation are shown in table 2.

2.1 WIMP discovery limits: statistical approach

In this section we describe the statistical procedure adopted for the determination of WIMP discovery limits, which follows a frequentist significance test using a likelihood ratio as a test statistic [59]. As a tool for the determination of WIMP discovery limits, this technique was first used in ref. [12] and subsequently in refs. [14, 17, 34, 60, 61]. In general, both the calculation of signal (WIMP) and background (CEνNS) events may involve nuisance parameters. We consider them only in the latter, assuming that they originate from uncertainties on the normalization of neutrino fluxes alone (section 3.2) or combined with: (i) measured CEνNS cross section uncertainties (section 3.1.1), (ii) point-neutron distribution mean-square-radius uncertainties (section 3.1.2), (iii) weak mixing angle uncertainties (section 3.1.2).

The general likelihood function we adopt depends on WIMP parameters (m_χ and $\sigma_{n-\chi}$) as well as on the nuisance parameters associated with neutrino fluxes normalization factors (denoted ϕ_α, with $\alpha = 1, \cdots, n_\nu = 11$) and nuisance $\mathcal{P}$, with $\mathcal{P} = \{n_\sigma,\ \mathcal{R},\ \Theta\}$ ($\mathcal{R}$ and Θ refer to the R_n and $\sin^2\theta_W$ nuisance parameters, while n_σ stands for the ratio between the experimentally measured CEνNS cross section and its SM theoretical value)

$$\mathcal{L}(m_\chi, \sigma_{\chi-n}, \Phi, \mathcal{P}) = \prod_{i=1}^{n_{\rm bins}} P(N_{\rm Exp}^i, N_{\rm Obs}^i) G(\mathcal{P}_i, \mu_{\mathcal{P}_i}, \sigma_{\mathcal{P}_i})$$
$$\times \prod_{\alpha=1}^{n_\nu} G(\phi_\alpha, \mu_\alpha, \sigma_\alpha)\,, \tag{2.11}$$

with $\Phi = (\phi_1, \cdots, \phi_{n_\nu})$. For the data-driven analysis $n_{\rm bin}$ is dictated by COHERENT data, so $n_{\rm bin} = 12$ for CsI and $n_{\rm bin} = 3$ for LAr [21, 23]. For the remaining analyses we consider $n_{\rm bins} = 100$. $P(x, n)$ and $G(x, \mu, \sigma)$ are Poisson and Gaussian probability distribution functions, respectively. This means that $N_{\rm Obs}$ is assumed to be a Poissonian random variable and that the nuisance parameters follow instead Gaussian distributions that parametrize their

Parameter ($\mathcal{P}$)	Mean (μ)	Unc. (standard deviation)
$\mathcal{R}$	4.78 fm	10%
Θ	0.2387	10%

Table 3. Mean and standard deviation for the nuisance parameters associated with the point-neutron mean-square-radius R_n and weak mixing angle $\sin^2\theta_W$ analyses.
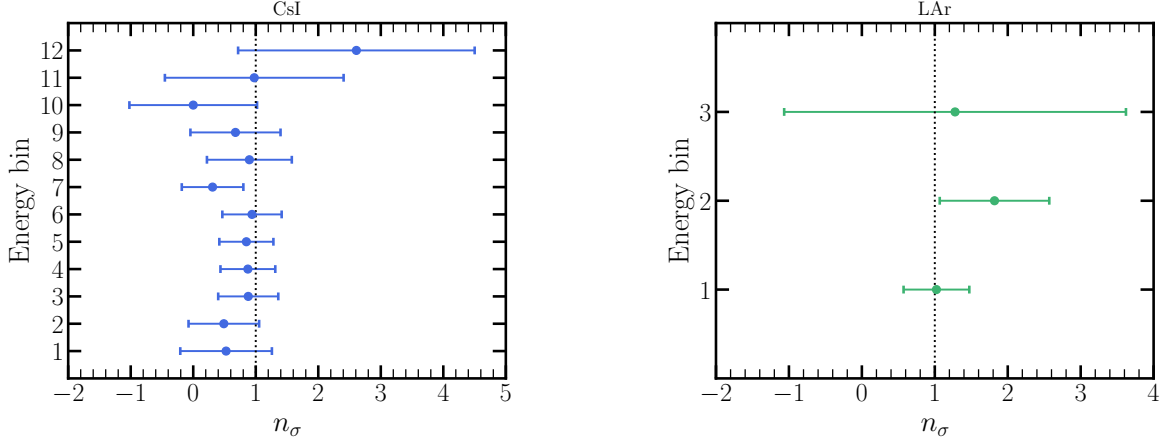

Figure 2. Experimentally measured CEνNS cross section normalized to the SM prediction (n_σ), extracted from COHERENT CsI and LAr data [21, 23]. Results in each recoil energy bin indicate the central value (mean) alone with its uncertainty ($1\,\sigma$ CL). They are used in the data-driven analysis profile likelihood ratio test in section 3.1.1.

uncertainties. The means μ_α and standard deviations σ_α are given by the normalization factors and uncertainties shown in table 1, while those for the nuisance parameters in the set $\mathcal{P}$ are given in table 3 and figure 2. Note that in the likelihood function in eq. (2.11) the Gaussian factors associated with the nuisance variables in the set $\mathcal{P}$ are bin-dependent. This is relevant for the data-driven analysis since in that case the means and standard deviations are energy dependent. In the case of uncertainties related with R_n and $\sin^2\theta_W$ there is a single Gaussian bin-independent distribution which factors out. The resulting likelihood function in those cases thus resembles that used in ref. [17].

To set discovery limits one defines a null hypothesis H_0 (CEνNS background only) and an alternative hypothesis H_1 which involves the WIMP signal plus the CEνNS background. The likelihood function in eq. (2.11) is then specialized for the two cases, $\mathcal{L}_0$ for H_0 and $\mathcal{L}_1$ for H_1. In both, $N_{\mathrm{Obs}}^i = \sum_\alpha N_\nu^i(\Phi_\alpha, \mathcal{P}_i) + N_W^i(\mathcal{P}_i)$[3] (see eqs. (2.2) and (2.6)), where N_{Obs}^i refers to the total number of "observed" events in the i-th bin in a toy experiment defined by a parameter space point $\{m_\chi, \sigma_{\chi-n}\}$ and neutrino flux normalization factors as well as $\mathcal{P}$ fixed to their means (see tables 1, 3 and figure 2). For the generation of these toy experiments we scan over a 200×200 grid with $m_\chi \subset [10^{-2}, 10^3]$ GeV and $\sigma_{\chi-n} \subset [10^{-50}, 10^{-40}]$ cm^2. Note that the range over which the sum in the first term in N_{Obs}^i runs depends on the energy bin. In the first bins all neutrino fluxes contribute, but as the energy bin increases they start to reach their kinematic tail and switch off, leaving at $E_r = 10^2$ keV only the atmospheric flux contribution.

---

[3] N_W involves nuisances only in the case of varying R_n.
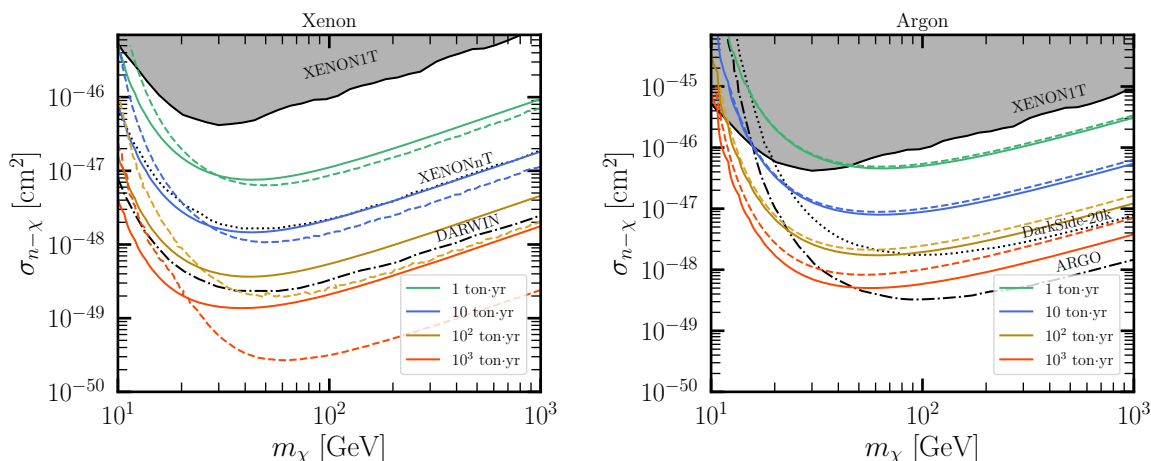
Figure 3. WIMP discovery limits obtained using the CEνNS cross section measurements at COHER-ENT with the CsI (left graph) and LAr (right graph) detectors [21, 23] (dashed curves). In addition to the nuisance parameters due to uncertainties on the neutrino flux normalizations, the results include bin-dependent nuisance parameters associated with the CEνNS cross section uncertainty as shown in figure 2. The current constraint set by XENON1T is shown in both panels. Moreover, we show as for comparison future sensitivities expected at LXe experiments XENONnT and DARWIN (left panel) [9, 10] and at LAr experiments DarkSide-20k and ARGO (right panel) [62, 63].

For $\mathcal{L}_0$ and in the i-th bin the "expected" number of events is given by $N_{\text{Exp}}^i = N_\nu^i(\Phi_\alpha, \mathcal{P}_i)$, with $N_\nu^i(\Phi_\alpha, \mathcal{P}_i)$ again dictated by eq. (2.2) but with the neutrino flux normalizations as well as $\mathcal{P}$ parametrized in terms of their nuisance variables. For $\mathcal{L}_1$ we make use of a useful element of the statistical method pointed out by Cowan et al. in ref. [59], namely the Asimov data set. According to the latter, it holds that $N_{\text{Exp}}^i = N_{\text{Obs}}^i$, while in the Gaussian factors the nuisance variables are fixed to their central values. One then calculates $\mathcal{L}_0$ and $\mathcal{L}_1$ for each parameter space point and then minimizes $-\mathcal{L}_0$ (or maximizes $\mathcal{L}_0$) for each nuisance variable. For each parameter space point (toy experiment) one evaluates the likelihood ratio (test statistics)

$$\lambda(0) = \frac{\mathcal{L}_0}{\mathcal{L}_1} \ . \tag{2.12}$$

This ratio quantifies the disagreement between the null and alternative hypotheses (or in other words it quantifies the significance of the WIMP signal), through the *equivalent significance* defined according to $Z = \sqrt{-2 \ln \lambda(0)}$. The *discovery limit* then follows by finding *the smallest WIMP cross section for which* 90% *of experiments have a WIMP signal above* 3σ. In terms of the equivalent significance this translates into $Z \geq 3$.

With these ingredients we are now in a position to proceed with the discussion of the effects on discovery limits due to uncertainties on the measured CEνNS cross section, R_n, $\sin^2 \theta_W$ and new interactions.

3 WIMP searches

3.1 WIMP searches in the presence of standard neutrino background

3.1.1 Data-driven analysis

In the "standard" calculation of WIMP discovery limits the CEνNS cross section is assumed to be known with 100% accuracy [12]. Uncertainties due to nuclear form factors or other quantities such as the weak mixing angle are not considered. Where the uncertainty on the cross section resides or whether there is new physics contributing to it — the subject of section 3.2 — is to a certain extent an assumption-dependent question. To avoid this a data-driven approach can be rather adopted, in which one uses the measured CEνNS cross section along with its uncertainty. This approach encapsulates all possible uncertainties the cross section can involve, regardless of assumptions.

To proceed, we first extract from the COHERENT CsI and LAr data the CEνNS cross section central values along with their standard deviations (the CsI data are directly applicable to xenon since both nuclides have about the same average mass and atomic numbers). To do so, we weigh the theoretical SM value of the CEνNS differential cross section with a multiplicative factor n_σ and use a spectral χ^2 test to fit n_σ in each recoil energy bin (see appendix A for details). Assuming that the CEνNS differential cross section uncertainty is fully encoded in a multiplicative factor is the most simple approach one can adopt. Given the quality of the data sets, the uncertainty could be assumed to be energy dependent. However, modeling such an energy-dependent uncertainty seems to us more arbitrary (there is a few number of functions one could use) than assuming a flat uncertainty.

For the data-driven analysis with COHERENT CsI data we use 12 bins starting at 7 photoelectrons (PE) and extending up to 29 PE (PE = $1.17\,E_r/\mathrm{keV}_{\mathrm{nr}}$) [21], while for the LAr dataset we use three bins starting at $5\,\mathrm{keV}_{\mathrm{ee}}$ and up to $25\,\mathrm{keV}_{\mathrm{ee}}$ ($\mathrm{keV}_{\mathrm{nr}} \simeq \mathrm{keV}_{\mathrm{ee}}/4$) [23]. Indeed, for energies above $25\,\mathrm{keV}_{\mathrm{ee}}$ the CEνNS event rate is small enough and the remaining bins are of little relevance. Note that in the definition of the χ^2 test, to extract the n_σ factors, systematic errors associated to neutrino flux and form factor uncertainties have been included as nuisance parameters. The results presented in figure 2 thus encode only uncertainties due to the cross section (indirect) measurement.

Exploiting this determination of the uncertainties on the CEνNS cross section from COHERENT data we then compute the WIMP discovery limits. We use the general definition of the likelihood function in eq. (2.11) along with the results depicted in figure 2. This implies that the regions that can be covered correspond to those affected by DSNB and sub-GeV atmospheric neutrino backgrounds (heavy WIMP masses). The results are displayed in figure 3, using CsI (LAr) data in the left (right) panel. In the analysis with CsI data one can see that in general, compared with the SM expectation (solid curves), WIMP discovery limits improve. A closer inspection to the left graph in figure 2 allows to understand this behavior. Except for bin number 12, the measured CEνNS cross section (central values) is smaller than the SM expectation, thus resulting in a background depletion which becomes more visible with increasing exposure. However, for low WIMP masses, $m_\chi \lesssim 20\,\mathrm{GeV}$, our likelihood analysis tends to favor the maximum cross section values, hence leading to a poorer sensitivity compared to the pure SM case.

Results derived using the LAr data behave instead the other way around. The data trend is that of a measured CEνNS cross section exceeding its SM expectation, as can be seen in the right graph of figure 2. Departures, however, are not substantial and thus the
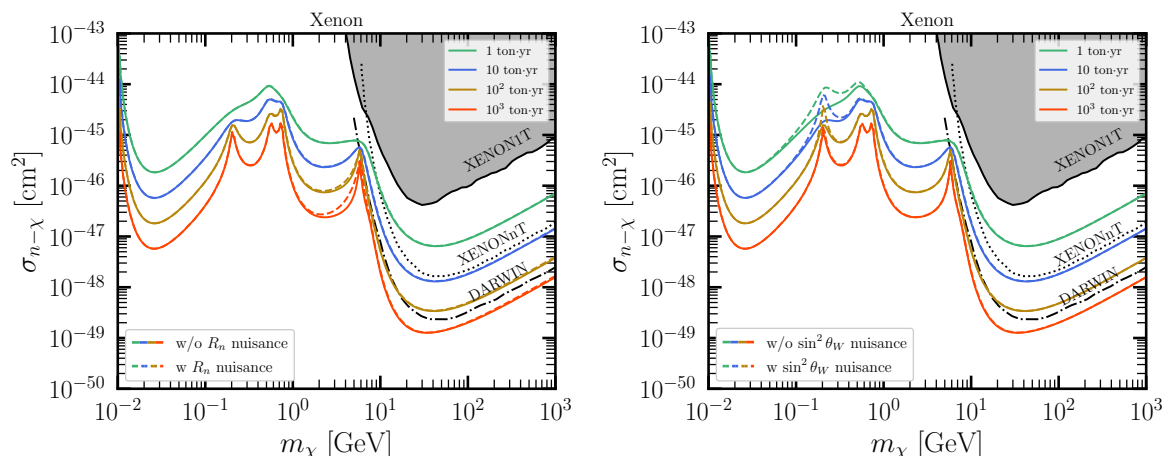
Figure 4. *Left graph*: WIMP discovery limit calculated by considering neutrino flux uncertainties as well as uncertainties on the xenon neutron distribution mean-square-radius. Results are presented for four different exposures and are compared with results obtained solely by considering neutrino flux uncertainties (solid curves). XENON1T, XENONnT and DARWIN sensitivities are shown for comparison [8–10]. *Right graph*: WIMP discovery limits calculated by considering uncertainties on the weak mixing angle at low energies.

enhancement of the background is not that large. As a result, discovery limits are only slightly worsen as shown in the left graph in figure 3.

Further data from CEνNS experiments will allow an improvement of the discovery limit we have presented here. Larger statistics combined with a better understanding of systematic and statistical uncertainties (as expected in future reactor and COHERENT experiments), will allow for a less spread CEνNS cross section measurement. However, even if statistics becomes abundant and uncertainties are shrinked to values below the percent level, neutrino flux uncertainties will still affect the exact position and shape of the neutrino floor. Improvements of the discovery limit will require therefore not only better measurements of the CEνNS cross section but of relevant neutrino fluxes, in particular those from the ^{8}B component.

3.1.2 Impact of nuclear form factor and weak mixing angle uncertainties

In contrast to proton distributions, neutron distributions are poorly known. With the exception of neutron distributions for ^{208}Pb — measured with high accuracy using parity violating electron scattering by the PREX experiment [64, 65] — and more recently for ^{133}Cs and ^{127}I using COHERENT data [66, 67], little is known about neutron distributions for other nuclei. Given the typical incoming neutrino energies for which CEνNS can be observed, nuclear effects are not as sizable as they are for other neutrino scattering processes such as e.g. quasi-elastic scattering or resonant pion production (see e.g. [68]). This, however, does not mean that they can be fully ignored.

Differences between proton and neutron distributions are expected to be substantial for neutron-rich nuclei. These departures have in turn an impact on the values the nuclear form factor can have at a particular momentum transfer [18]. At very low q — typical of reactor or solar neutrino fluxes — deviations are small and so have little impact on the neutrino event spectrum. As q increases to larger values — typical of stopped-pion or sub-GeV atmospheric neutrino fluxes — uncertainties on the point-neutron distribution mean-square radius become

relevant and can have an impact. Note that this effect applies as well to the WIMP event rate, so not only the CEνNS event spectrum comes along with an uncertainty but also the WIMP event spectrum. However, in contrast to the WIMP rate, which involves as well uncertainties due to astrophysical parameter inputs, nuclear physics uncertainties entirely determine the precision with which CEνNS can be precisely predicted.

The weak-charge form factor in eq. (2.3) can be written according to [69]

$$
\begin{aligned}
F_W \simeq \frac{1}{Q_W} &\left[Z \left(g_V^p - \frac{g_V^p}{6} r_p^2 q^2 - \frac{g_V^n}{6} r_n^2 q^2 \right) F_p(q^2) \right. \\
&\left. + N \left(g_V^n - \frac{g_V^n}{6} r_p^2 q^2 - \frac{g_V^p}{6} r_n^2 q^2 \right) F_n(q^2) \right] ,
\end{aligned}
\tag{3.1}
$$

where the spin-independent proton and neutron nuclear form factors are normalized, $F_p(q^2 = 0) = 1$ and $F_n(q^2 = 0) = 1$. The quantities in front of the nuclear form factors are the leading-order nucleon form factor terms. Given the momentum transfer values we are dealing with, in our analysis we keep only the q^2-independent terms. Including order q^2 terms will correct our results at the percent level in the atmospheric neutrino region (heavy WIMP mass region), which, given the expected neutrino event rate (statistics), is too small to yield a sizable effect [53]. Note that in eq. (2.7) the same assumption has been adopted, in addition to the assumption of a WIMP isospin-conserving interaction.

As we have pointed out, we adopt the Helm parametrization for the spin-independent proton and neutron nuclear form factors. It relies on the assumption that nucleon distributions follow from a convolution of an uniform distribution of radius R_0 (diffraction radius) and a Gaussian profile, characterized by the folding width s that accounts for the surface thickness. The Helm form factor is then given by

$$
F(q^2) = 3 \frac{j_1(qR_0)}{qR_0} e^{-\frac{1}{2}(qs)^2} ,
\tag{3.2}
$$

where $j_1(x)$ is a spherical Bessel function of the first type and $s = 0.9\,\mathrm{fm}$ [70]. The diffraction radius is determined by the mean-square radius of the corresponding distribution according to

$$
R_0 = \sqrt{\frac{5}{3} \left(R_X^2 - 3s^2 \right)} \qquad (X = p, n) .
\tag{3.3}
$$

Compared with the form factor parametrization based on the symmetrized Fermi distribution and the Klein-Nystrand parametrization [71, 72], the Helm parametrization tends to underestimate event rates [52]. For momentum transfer values as those implied by sub-GeV atmospheric neutrino fluxes (heavy WIMP masses), event rates interpolate between values determined by the Helm and the Klein-Nystrand form factors with variations of order 10%. So, for definiteness we choose to work with the Helm parametrization understanding that event rates for both WIMP and neutrinos fluctuate by about 10%.

In the statistical analysis, we calculate N_{Obs}^i by fixing R_p to its averaged value calculated according to $R_p = \sum_{i=1}^9 X_i R_p^i$, where X_i refers to the relative abundance of the i-th xenon stable isotope and R_p^i to its proton distribution root-mean-square radius extracted from ref. [73]. We obtain the averaged value reported in table 3. For the averaged neutron distribution root-mean-square radius we use $R_n = R_p = \mathcal{R}$. We then allow 10% variations above this value in the Poisson and Gaussian factors in $\mathcal{L}_0$. We then calculate the equivalent significance for each parameter space point and after imposing $Z \geq 3$ we get the discovery

limit determined not only by neutrino flux uncertainties but also by uncertainties on the xenon neutron distribution mean-square radius (nuclear form factor uncertainty).

The result is shown in the left graph of figure 4. One can see that for low WIMP masses there is no difference between the result obtained by considering neutrino flux uncertainties alone (solid curves) and the result including additional neutron distribution mean-square radius uncertainties (dashed curves). This is expected since for those WIMP masses and incoming neutrino energies, the zero momentum transfer limit is a rather good approximation. Form factor effects are thus negligible. As the WIMP mass increases and so the incoming neutrino energy, the effect starts to show up and becomes more pronounced as exposure increases. The region in WIMP mass where sizable deviations are observed corresponds to regions where the dominant background is determined by ^{8}B and hep neutrino fluxes. In that region the typical momentum transfer is of the order of 30–40 MeV, for which the form factor spread is of the order of 2–3% [18]. At low exposure, the size of the uncertainty combined with a mild statistics leads to an effect which can be barely noted. However, as exposure increases (and so statistics) the effect becomes more prominent.

The variation of the WIMP discovery limit due to the form factor uncertainty is also expected. With increasing neutron mean-square radius, nuclear size increases. A larger nuclear radius in turn means that the loss of coherence happens for smaller q. As R_n increases, up to the 10% above R_p, the number of neutrino events decreases and so the WIMP event rate. The overall effect is that of a diminished discovery limit at high exposures, though rather feeble. For increasing WIMP masses and neutrino energies (entering the atmospheric neutrino region), form factor uncertainties increase up to the order of 5%, but statistics becomes scarce even for the maximum exposure that we have chosen. As a result, the discovery limit at high WIMP masses becomes insensitive to this effect. One can fairly conclude that uncertainties on the WIMP and neutrino event rates originating from the xenon neutron distribution mean-square radius have little impact on the WIMP discovery limit. The reason behind this behavior is first of all related with the fact that nuclear form factor uncertainties in xenon are *per se* small [18]. It is secondly related with another fact: once R_n increases, both the neutrino background and the WIMP event rate are (slightly) suppressed.

We now turn to the discussion of uncertainties on the low-energy value of the weak mixing angle. The best measurement of $\sin^2 \theta_W$ has been done at the Z scale at Tevatron, LEP and more recently at the LHC (see e.g. [74]). The precision of those measurements is of the order of $\sim 0.1\%$. At other (lower) scales — that span about five orders of magnitude — measurements include NuTeV, parity violation in electron scattering, electron and proton weak charge and atomic parity violation [75–79]. In contrast to measurements at the Z scale, these measurements involve order $\sim 10\%$ uncertainties.

Lacking the precision of accelerator experiments, these measurements still allow variations of the weak mixing angle that can have an impact on WIMP discovery limits. However, for this to be the case a large CEνNS statistics is required given that $g_V^p \ll g_V^n$. This means that effects of weak mixing angle uncertainties are expected to be relevant at low WIMP masses, where solar neutrino fluxes are more abundant.

As in the nuclear form factor case, this effect is also — in principle — energy dependent. At each WIMP mass there is a neutrino flux that matters, and therefore a $q_{\max} = \sqrt{2 m_N E_r^{\max}}$ that fixes the renormalization scale at which $\sin^2 \theta_W$ should be evaluated. In other words, as m_χ increases the mean value for $\sin^2 \theta_W$ changes since the renormalization scale does so. There is however an interesting observation that allows for the following simplification: for
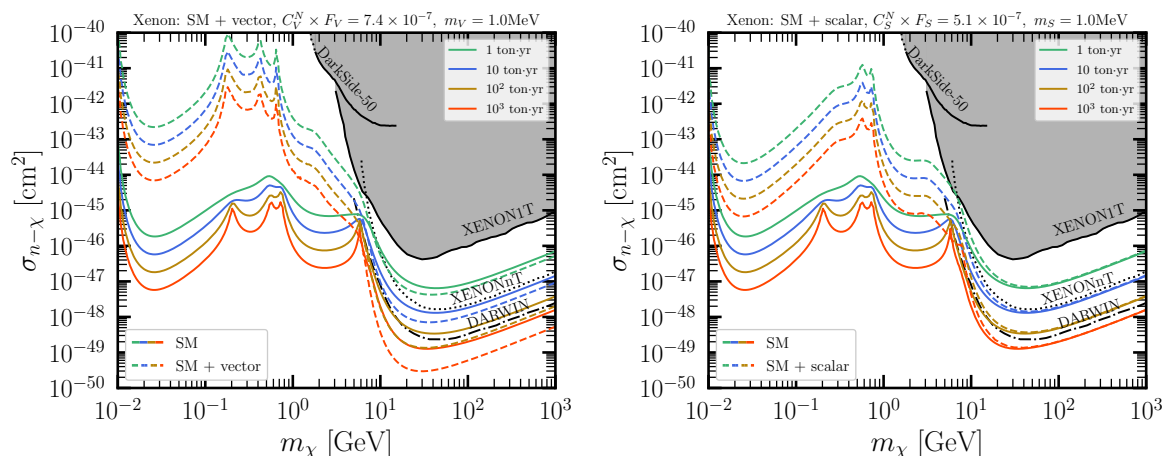
Figure 5. *Left graph*: WIMP discovery limit in the presence of a long-range vector interaction calculated for four different exposures and for values of the coupling and vector boson mass fixed to maximize its effect. Along with the result (dashed curves), the SM discovery limits (solid curves) are shown for comparison. *Right graph*: same as for left graph but for a long-range scalar interaction. Couplings and masses have been fixed as required by COHERENT CsI data [30], they correspond to the 90% CL upper bounds. In both panels we also show for comparison the upper limits set by XENON1T and DarkSide-50 [5, 8, 81], together with future sensitivities for XENONnT and DARWIN [9, 10].

the renormalization scales (q_{max}) that matter in the calculation of WIMP discovery limits ($q_{max} \lesssim 200\,\mathrm{MeV}$), the weak mixing angle RGE evolution (in the SM) is rather flat [80]. One can then fix its mean value to its zero momentum transfer value obtained by extrapolation [50]

$$\sin^2 \theta_W(q=0) = \kappa(q=0)_{\overline{\mathrm{MS}}} \sin^2 \theta_W(m_Z)_{\overline{\mathrm{MS}}}, \qquad (3.4)$$

where the parameter at $q=0$ is given by $\kappa(q=0)_{\overline{\mathrm{MS}}} = 1.03232 \pm 0.00029$ and the weak mixing angle at the Z scale by $\sin^2 \theta_W(m_Z)_{\overline{\mathrm{MS}}} = 0.23122 \pm 0.00003$ [74]. Taking the central values and allowing for a 10% uncertainty one can then calculate the WIMP discovery limits obtained by combining neutrino flux normalization and weak mixing angle uncertainties. The result is displayed in the right graph of figure 4. As expected, the effect of the weak mixing angle uncertainty becomes visible at low WIMP masses. The region where sizable deviations from the "standard" result are more pronounced corresponds to those where the pp, ^{7}Be (two lines) and ^{13}N dominate the background. Note that once less abundant neutrino fluxes kick in (from ^{8}B on) the discovery limit converges to the "standard" result. The reason is the combination of a small effect and low statistics.

Overall, the behavior of the discovery limit in the presence of this uncertainty can be readily understood. As the weak mixing angle increases, the coherent weak charge becomes more negative. Quadratically, the coupling increases (decreases) about $\sim 12\%$ when allowing the weak mixing angle to increase (decrease) by 10%. Although the enhancement is not dramatically large, it is sufficient to increase the number of neutrino events.

3.2 WIMP searches in the presence of non-standard neutrino background

As far as we know, new physics in neutrino backgrounds at multi-ton DM detectors have been discussed using the so-called *one neutrino event contour line* in refs. [24–28, 30]. Analyses

aiming at determining the impact of the new interactions on WIMP discovery limits have been instead presented in refs. [25, 34, 82, 83], using neutrino nonstandard interactions (NSI) as the new physics contribution. Here we first revisit results for interactions including light vector and scalar mediators, and then we present new results considering neutrino magnetic moments/transitions.

In the light of COHERENT data and of other forthcoming CEνNS experiments [21, 23, 84–87], light vector mediators have been the subject of recent analyses (see e.g. [88, 89]). In the presence of a new vector lepton flavor-conserving interaction the CEνNS differential cross follows from eq. (2.3) by shifting the coherent weak charge Q_W according to

$$Q_V = Q_W + \frac{C_V^N F_V}{\sqrt{2} G_F (2 m_N E_r + m_V^2)} \, , \tag{3.5}$$

where m_V is the mass of the vector mediator while the coupling F_V determines the strength at which the vector couples to neutrinos through vector and axial couplings. The coupling C_V^N, instead, determines the coupling of the new vector boson to the nucleus

$$C_V^N = (A - Z)(h_V^u + 2 h_V^d) + Z(2 h_V^u + h_V^d) \, , \tag{3.6}$$

with h_V^q the vector current couplings of the vector boson to up and down quarks (compared with the vector current, the axial current is suppressed and so no axial couplings are included). From the structure of the new weak charge, it is clear that the new interaction can either constructively or destructively interfere with the SM contribution. The presence of a new vector interaction can therefore enhance or deplete the SM contribution and depending on the momentum transfer, $q^2 = 2 m_N E_r$, can lead to spectral distortions as well [89, 90].

In order to maximize the effects implied by the new interaction we fix the product of couplings $C_V^N F_V$ to their maximum allowed value according to COHERENT CsI data at $m_V = 1\,\text{MeV}$ [30]: $C_V^N F_V \lesssim 7.4 \times 10^{-7}$ at the 90% CL.[4] Note that this value applies to CsI, but can be used for xenon as well given the similarity of these nuclides. Light vector mediators are subject to constraints that follow from stellar cooling arguments and neutrino diffusion time disruption in supernova environments [91–93]. The combination of coupling and mass that we have chosen is reconcilable with these bounds.

We then calculate the WIMP discovery limit. In this case the only nuisance parameters are those associated with neutrino flux normalization factors. However, depending on the transfer momentum, the new contribution can enhance (deplete) the neutrino background thus worsening (improving) the discovery limit. This is confirmed by the result shown in the left graph of figure 5.

At low WIMP masses the discovery limit is diminished by several orders of magnitude. This can be readily understood by the q^2 dependence of the new contribution. At low momentum transfer this term is enhanced and overcomes the SM contribution, as the CEνNS cross section is enhanced towards low momentum transfer regions. As a result, the neutrino background increases, thus leading to a dramatic diminishing of the discovery limit. For regions above 10 GeV, after the ^{8}B and hep neutrino fluxes reach their kinematic tail, the discovery limit improves. This crossover can be understood as follows. The SM coherent weak charge is negative, while the new contribution is positive. So, as q^2 increases the new

---

[4]Statistically the observation of CEνNS with the CsI detector is more robust than with the LAr detector. In the former, data favors the observation of the signal over background at the 6.7σ CL, while in the latter at the 3σ CL [21, 23]. That is why we use constraints derived using CsI data [30].
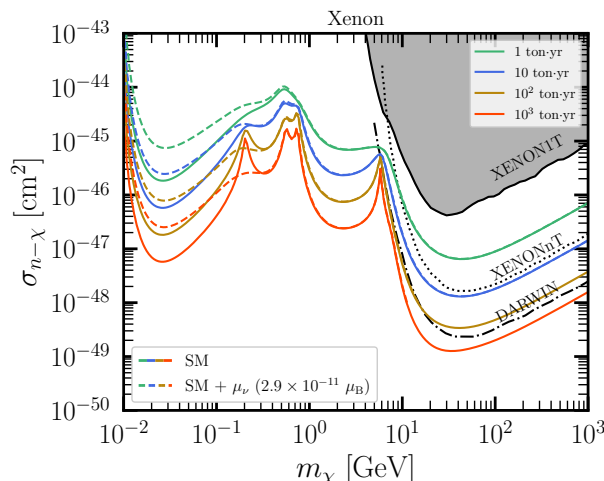
Figure 6. WIMP discovery limits in the presence of neutrino magnetic/transition interactions along with discovery limits in the SM alone. The neutrino magnetic moment has been fixed to $2.9 \times 10^{-11} \mu_B$, the 90% CL upper limit reported by the GEMMA reactor experiment [94].

contribution becomes less prominent and destructively interferes with the SM term, leading to a suppression of Q_V. The background then becomes less severe, thus resulting in an improvement of the discovery limit.

Scalar interactions in both the effective and light regimes have been as well recently considered in the context of CEνNS related experiments [95–97]. Since the scalar coupling involves a chirality flip it cannot (sizably) interfere with the SM contribution, in contrast to the vector interaction. Thus, in the presence of the scalar coupling, the CEνNS cross section consists of two terms, the SM term in eq. (2.3) and a second term given by (assuming universal lepton flavor couplings) [30, 95, 98]

$$\frac{d\sigma_S}{dE_r} = \frac{G_F^2}{2\pi} m_N Q_S^2 \frac{m_N E_r}{2E_\nu^2} F^2(q^2) \,, \tag{3.7}$$

where the scalar charge Q_S reads

$$Q_S = \frac{C_S^N F_S}{G_F(2m_N E_r + m_S^2)} \,. \tag{3.8}$$

Here, F_S measures the strength at which the scalar couples to neutrinos through scalar and pseudoscalar couplings, and C_S^N determines the coupling of the scalar to the nucleus according to

$$C_S^N = (A - Z) \sum_{q=u,d} h_S^q \frac{m_n}{m_q} f_{T_q}^n + Z \sum_{q=u,d} h_S^q \frac{m_p}{m_q} f_{T_q}^p \,, \tag{3.9}$$

with h_S^q being the couplings of the scalar to up and down quarks. The hadronic form factors $f_{T_q}^{n,p}$ follow from chiral perturbation theory calculations using measurements of the π-nucleon sigma term. Their values can be found in e.g. [99, 100].

Results for the impact of this interaction on WIMP discovery limits are shown in the right graph of figure 5. As in the vector case, the product $C_S^N F_S$ has been fixed to its maximum allowed value at $m_S = 1\,\mathrm{MeV}$ according to COHERENT CsI data: $C_S^N F_S \lesssim 5.1 \times 10^{-7}$ at the 90% CL. This value is consistent with astrophysical and cosmological bounds

– 16 –

as well as with bounds derived from neutrino masses, which are generated by the scalar coupling below $\Lambda_{\rm QCD}$ [30]. The results follow expectations. The scalar contribution peaks towards the low momentum transfer region (low WIMP mass region), thus enhancing the background and so worsening the discovery limit. One can see that the degree at which the discovery limit is affected is less severe than in the vector case. This is also expected, since the leading vector term is linear in the coupling while the scalar contributes quadratically. At high momentum transfer (high WIMP mass) the scalar keeps enhancing the background, hence there is no crossover as in the vector case. Since destructive interference is not possible in the scalar case, the discovery limit is still diminished at $m_\chi \gtrsim 10\,{\rm GeV}$, though less than in the low WIMP mass region due to the larger momentum transfer involved.

We finally move to the case of neutrino magnetic moments/transitions, which have been a subject of recent interest in the context of COHERENT data and multi-ton DM experiments [101–105]. The neutrino electromagnetic current can be parametrized in terms of four form factors which in the zero momentum transfer limit define the neutrino: electric charge, electric dipole moments (or transitions), magnetic dipole moments (or transitions) and anapole moments. These parameters enable the coupling of neutrinos to photons and so through t-channel processes they contribute to CEνNS and neutrino-electron elastic scattering (see [106] for a review). The new processes do not interfere with the SM contribution, so the total CEνNS cross section in the presence of a neutrino magnetic moment interaction consists of the SM term in eq. (2.3) and a new term given by [107]

$$\frac{d\sigma_\gamma}{dE_r} = \pi \alpha_{\rm em}^2 Z^2 \frac{\mu_{\rm eff}^2}{m_e^2} \left(\frac{1}{E_r} - \frac{1}{E_\nu} \right) F^2(q^2), \tag{3.10}$$

where $\alpha_{\rm em}$ is the fine structure constant and $\mu_{\rm eff}^2$ is an effective parameter (in Bohr magneton units μ_B) that encodes the neutrino magnetic and electric dipole moments (and transitions) along with neutrino oscillation probabilities [105, 108]. The main feature of the new coupling is spectral distortions, resulting from the fact that the cross section is forward peaked because of the Coulomb divergence (infinite range interaction). This means that one expects the WIMP discovery limit to be diminished at low WIMP masses (low momentum transfer region). Moreover, given the tight constraints on the coupling implied by searches at GEMMA, BOREXINO and TEXONO [94, 108, 109], the discovery limit is also expected to converge to the "standard" case as soon as the momentum transfer reaches larger values.

For the calculation of the impact of such interaction on WIMP discovery limits we have fixed $\mu_{\rm eff} = 2.9 \times 10^{-11} \mu_B$, which corresponds to the 90%CL reported by GEMMA [94] and XENON1T [110]. The result is displayed in figure 6, which shows along with the discovery limits implied by the new interaction the "standard" limits for comparison. One can see that up to WIMP masses of order $\sim 0.2\,{\rm GeV}$ the discovery limit worsens, because of the background enhancement induced by the neutrino magnetic moment contribution. As soon as one enters the region of large transfer momentum, the Coulomb divergence fades away and the discovery limit matches that of the SM alone.

4   Conclusions

With the advent of the DM multi-ton detectors era in mind and with well-established measurements of the CEνNS process by the COHERENT collaboration, we have reconsidered the case of WIMP discovery limits. We have adopted, for the first time, a data-driven analysis in which we have treated the CEνNS cross section as a parameter entirely determined

by experimental data. Using this approach, while taking into account neutrino flux uncertainties, we have derived WIMP discovery limits using the CsI and LAr COHERENT data sets [21, 23]. Our results are free from theoretical and phenomenological assumptions. They are also of particular interest for future experiments XENONnT, DARWIN, DarkSide-20k and ARGO, as they fall in the region where these experiments will have maximum sensitivities [8–10, 62, 63].

We have as well presented a more assumption-dependent analysis in which we have evaluated WIMP discovery limits by taken into account: (i) Nuclear form factor uncertainties, (ii) possible fluctuations of the weak mixing angle at low energies. Case (i) is driven by uncertainties on the xenon point-neutron distribution mean-square-radius. This quantity, in contrast to its proton counterpart, has not been measured and so implies a sizable uncertainty on both the WIMP and CEνNS event rates. We have shown that its effect on WIMP discovery limits, however, is mild and relevant only in the 1-10 GeV WIMP mass region, where mainly ^{8}B and hep neutrino backgrounds matter. In case (ii), the effect is only relevant for the CEνNS event rate and in regions of small WIMP masses, where statistics is large enough to allow the proton contribution to leave its imprint.

Additionally, we have presented a full model-dependent analysis aiming at illustrating the impact that new physics at the neutrino background level — lurking at low-scales — might have on WIMP discovery limits. We considered light vector and scalar mediators as well as neutrino magnetic moments/transitions. For a light vector mediator, we have found that its presence can worsen WIMP discovery limits by several orders of magnitude for WIMP masses up to ~ 10 GeV. From that point on, our results indicate a crossover where the new vector interaction actually leads to an improvement of the discovery limit, albeit mild. WIMP discovery limits in the presence of scalar and neutrino magnetic moment/transition interactions are always worsen, in particular in regions of light WIMPs.

Finally, we point out that searches for WIMPs using forthcoming multi-ton detector technologies require a precise understanding of WIMP discovery limits. In our view, this calls — ideally — for the most assumption-free determination of the effects of the neutrino background, for the inclusion of known sub-leading effects and the consideration of possible new physics effects. This has been the main goal of the analyses presented here.

Acknowledgments

A Extraction of CEνNS cross section from COHERENT data

The datasets available for the CsI and LAr COHERENT detectors provide spectral information on the measured number of CEνNS events and their uncertainties [111, 112]. Under the assumption that the experimental cross section is proportional to its theoretical prediction, the COHERENT collaboration has already provided a determination of the measured CEνNS cross section on argon as $\sigma_{\mathrm{meas}} = \frac{N_{\mathrm{meas}}}{N_{\mathrm{th}}}\sigma_{\mathrm{th}}$ (for details see ref. [113]), where N_{meas} and N_{th} are the total number of measured and theoretical events, respectively. Motivated by the latter, here we perform a similar analysis which in our case is applied independently for each energy bin by considering $\sigma^i_{\mathrm{meas}} = n^i_\sigma \, \sigma^i_{\mathrm{th}}$. Following this approach, we extract the measured cross section along with its uncertainty for both CsI and LAr datasets.

For the case of CsI we adopt the χ^2 function

$$\chi^2_i = \left[\frac{N^i_{\mathrm{exp}} - (1+\alpha)N^i_{\mathrm{meas}}(n^i_\sigma) - (1+\beta)B^i_{0\mathrm{n}}}{\sigma^i_{\mathrm{stat}}} \right]^2 + \left(\frac{\alpha}{\sigma_\alpha}\right)^2 + \left(\frac{\beta}{\sigma_\beta}\right)^2 , \tag{A.1}$$

where α and β are nuisance parameters which account for the uncertainty on the rate with $\sigma_\alpha = 28\%$ and on the prompt neutron background $B_{0\mathrm{n}}$ with $\sigma_\beta = 25\%$, respectively. Finally, the statistical uncertainty is defined as $\sigma^i_{\mathrm{stat}} = \sqrt{N^i_{\mathrm{exp}} + B^i_{0\mathrm{n}} + 2B^i_{\mathrm{ss}}}$, where B^i_{ss} denotes the steady state background (for details see ref. [111]). For the case of LAr, we focus on the *analysis-A* of COHERENT [23] and we follow the χ^2 function [114]

$$\chi^2_i = \frac{\left(N^i_{\mathrm{exp}} - \alpha N^i_{\mathrm{meas}}(n^i_\sigma) - \beta B^i_{\mathrm{PBRN}} - \gamma B^i_{\mathrm{LBRN}}\right)^2}{\left(\sigma^i_{\mathrm{exp}}\right)^2 + \left[\sigma_{\mathrm{BRNES}}\left(B^i_{\mathrm{PBRN}} + B^i_{\mathrm{LBRN}}\right)\right]^2} + \left(\frac{\alpha - 1}{\sigma_\alpha}\right)^2 + \left(\frac{\beta - 1}{\sigma_\beta}\right)^2 + \left(\frac{\gamma - 1}{\sigma_\gamma}\right)^2 .$$

Here, BRNES corresponds to the Beam Related Neutron Energy Shape, while PBRN (LBRN) represents the Prompt (Late) Beam-Related Neutron Background data with $\sigma_\beta = 32\%$ ($\sigma_\gamma = 100\%$) [112]. The remaining parameters: Beam Related Neutron Energy Shape (BRNES) uncertainty $\sigma_{\mathrm{BRNES}} = 1.7\%$ and the systematic uncertainty of the signal rate $\sigma_\alpha = 13.4\%$ are taken from the estimations of ref. [114].

References

[1] L. Baudis, *Direct dark matter detection: the next decade*, *Phys. Dark Univ.* **1** (2012) 94 [arXiv:1211.7222] [INSPIRE].

[2] LUX collaboration, *Improved limits on scattering of weakly interacting massive particles from Reanalysis of 2013 LUX Data*, *Phys. Rev. Lett.* **116** (2016) 161301 [arXiv:1512.03506] [INSPIRE].

[3] PANDAX-II collaboration, *Dark matter results from 54-ton-day exposure of PandaX-II Experiment*, *Phys. Rev. Lett.* **119** (2017) 181302 [arXiv:1708.06917] [INSPIRE].

[4] XENON collaboration, *Light dark matter search with ionization signals in XENON1T*, *Phys. Rev. Lett.* **123** (2019) 251801 [arXiv:1907.11485] [INSPIRE].

[5] DARKSIDE collaboration, *DarkSide-50 532-day dark matter search with low-radioactivity argon*, *Phys. Rev. D* **98** (2018) 102006 [arXiv:1802.07198] [INSPIRE].

[6] DEAP collaboration, *Search for dark matter with a 231-day exposure of liquid argon using DEAP-3600 at SNOLAB*, *Phys. Rev. D* **100** (2019) 022004 [arXiv:1902.04048] [INSPIRE].

[7] LUX-ZEPLIN collaboration, *Projected WIMP sensitivity of the LUX-ZEPLIN dark matter experiment*, *Phys. Rev. D* **101** (2020) 052002 [arXiv:1802.06039] [INSPIRE].

[8] XENON collaboration, *Physics reach of the XENON1T dark matter experiment*, *JCAP* **04** (2016) 027 [arXiv:1512.07501] [INSPIRE].

[9] DARWIN collaboration, *DARWIN: towards the ultimate dark matter detector*, *JCAP* **11** (2016) 017 [arXiv:1606.07001] [INSPIRE].

[10] XENON collaboration, *Projected WIMP sensitivity of the XENONnT dark matter experiment*, *JCAP* **11** (2020) 031 [arXiv:2007.08796] [INSPIRE].

[11] L.E. Strigari, *Neutrino coherent scattering rates at direct dark matter detectors*, *New J. Phys.* **11** (2009) 105011 [arXiv:0903.3630] [INSPIRE].

[12] J. Billard, L. Strigari and E. Figueroa-Feliciano, *Implication of neutrino backgrounds on the reach of next generation dark matter direct detection experiments*, *Phys. Rev. D* **89** (2014) 023524 [arXiv:1307.5458] [INSPIRE].

[13] J.B. Dent, B. Dutta, J.L. Newstead and L.E. Strigari, *Effective field theory treatment of the neutrino background in direct dark matter detection experiments*, *Phys. Rev. D* **93** (2016) 075018 [arXiv:1602.05300] [INSPIRE].

[14] F. Ruppin, J. Billard, E. Figueroa-Feliciano and L. Strigari, *Complementarity of dark matter detectors in light of the neutrino background*, *Phys. Rev. D* **90** (2014) 083510 [arXiv:1408.3581] [INSPIRE].

[15] S.E. Vahsen, C.A.J. O'Hare and D. Loomba, *Directional recoil detection*, *Ann. Rev. Nucl. Part. Sci.* **71** (2021) 189 [arXiv:2102.04596] [INSPIRE].

[16] J.H. Davis, *Dark matter vs. neutrinos: the effect of astrophysical uncertainties and timing information on the neutrino floor*, *JCAP* **03** (2015) 012 [arXiv:1412.1475] [INSPIRE].

[17] C.A.J. O'Hare, *Dark matter astrophysical uncertainties and the neutrino floor*, *Phys. Rev. D* **94** (2016) 063527 [arXiv:1604.03858] [INSPIRE].

[18] D. Aristizabal Sierra, J. Liao and D. Marfatia, *Impact of form factor uncertainties on interpretations of coherent elastic neutrino-nucleus scattering data*, *JHEP* **06** (2019) 141 [arXiv:1902.07398] [INSPIRE].

[19] D.K. Papoulias, T.S. Kosmas, R. Sahu, V.K.B. Kota and M. Hota, *Constraining nuclear physics parameters with current and future COHERENT data*, *Phys. Lett. B* **800** (2020) 135133 [arXiv:1903.03722] [INSPIRE].

[20] M. Hoferichter, J. Menéndez and A. Schwenk, *Coherent elastic neutrino-nucleus scattering: EFT analysis and nuclear responses*, *Phys. Rev. D* **102** (2020) 074018 [arXiv:2007.08529] [INSPIRE].

[21] COHERENT collaboration, *Observation of coherent elastic neutrino-nucleus scattering*, *Science* **357** (2017) 1123 [arXiv:1708.01294] [INSPIRE].

[22] COHERENT collaboration, *COHERENT Collaboration data release from the first observation of coherent elastic neutrino-nucleus scattering*, arXiv:1804.09459 [INSPIRE].

[23] COHERENT collaboration, *First measurement of coherent elastic neutrino-nucleus scattering on argon*, *Phys. Rev. Lett.* **126** (2021) 012002 [arXiv:2003.10630] [INSPIRE].

[24] B. Dutta, S. Liao, L.E. Strigari and J.W. Walker, *Non-standard interactions of solar neutrinos in dark matter experiments*, *Phys. Lett. B* **773** (2017) 242 [arXiv:1705.00661] [INSPIRE].

[25] E. Bertuzzo, F.F. Deppisch, S. Kulkarni, Y.F. Perez Gonzalez and R. Zukanovich Funchal, *Dark matter and exotic neutrino interactions in direct detection searches*, *JHEP* **04** (2017) 073 [arXiv:1701.07443] [INSPIRE].

[26] D. Aristizabal Sierra, N. Rojas and M.H.G. Tytgat, *Neutrino non-standard interactions and dark matter searches with multi-ton scale detectors*, *JHEP* **03** (2018) 197 [arXiv:1712.09667] [INSPIRE].

[27] C. Bœhm, D.G. Cerdeño, P.A.N. Machado, A. Olivares-Del Campo, E. Perdomo and E. Reid, *How high is the neutrino floor?*, *JCAP* **01** (2019) 043 [arXiv:1809.06385] [INSPIRE].

[28] R. Essig, M. Sholapurkar and T.-T. Yu, *Solar neutrinos as a signal and background in direct-detection experiments searching for Sub-GeV dark matter with electron recoils*, *Phys. Rev. D* **97** (2018) 095029 [arXiv:1801.10159] [INSPIRE].

[29] P.B. Denton, Y. Farzan and I.M. Shoemaker, *Testing large non-standard neutrino interactions with arbitrary mediator mass after COHERENT data*, *JHEP* **07** (2018) 037 [arXiv:1804.03660] [INSPIRE].

[30] D. Aristizabal Sierra, B. Dutta, S. Liao and L.E. Strigari, *Coherent elastic neutrino-nucleus scattering in multi-ton scale dark matter experiments: classification of vector and scalar interactions new physics signals*, *JHEP* **12** (2019) 124 [arXiv:1910.12437] [INSPIRE].

[31] J. Monroe and P. Fisher, *Neutrino backgrounds to dark matter searches*, *Phys. Rev. D* **76** (2007) 033007 [arXiv:0706.3019] [INSPIRE].

[32] J.D. Vergados and H. Ejiri, *Can solar neutrinos be a serious background in direct dark matter searches?*, *Nucl. Phys. B* **804** (2008) 144 [arXiv:0805.2583] [INSPIRE].

[33] A. Gutlein et al., *Solar and atmospheric neutrinos: Background sources for the direct dark matter search*, *Astropart. Phys.* **34** (2010) 90 [arXiv:1003.5530] [INSPIRE].

[34] M.C. Gonzalez-Garcia, M. Maltoni, Y.F. Perez-Gonzalez and R. Zukanovich Funchal, *Neutrino discovery limit of dark matter direct detection experiments in the presence of non-standard interactions*, *JHEP* **07** (2018) 019 [arXiv:1803.03650] [INSPIRE].

[35] C. Giunti and C. W. Kim, *Fundamentals of neutrino physics and astrophysics*, Oxford University Press (2007).

[36] N. Vinyoles et al., *A new generation of standard solar models*, *Astrophys. J.* **835** (2017) 202 [arXiv:1611.09867] [INSPIRE].

[37] J.F. Beacom, *The diffuse supernova neutrino background*, *Ann. Rev. Nucl. Part. Sci.* **60** (2010) 439 [arXiv:1004.3311] [INSPIRE].

[38] M. Honda, M. Sajjad Athar, T. Kajita, K. Kasahara and S. Midorikawa, *Atmospheric neutrino flux calculation using the NRLMSISE-00 atmospheric model*, *Phys. Rev. D* **92** (2015) 023004 [arXiv:1502.03916] [INSPIRE].

[39] SNO collaboration, *Combined analysis of all three phases of solar neutrino data from the sudbury neutrino observatory*, *Phys. Rev. C* **88** (2013) 025501 [arXiv:1109.0763] [INSPIRE].

[40] BOREXINO collaboration, *First simultaneous precision spectroscopy of pp, ^7Be, and pep solar neutrinos with Borexino Phase-II*, *Phys. Rev. D* **100** (2019) 082004 [arXiv:1707.09279] [INSPIRE].

[41] SNO collaboration, *A search for neutrinos from the solar hep reaction and the diffuse supernova neutrino background with the sudbury neutrino observatory*, *Astrophys. J.* **653** (2006) 1545 [hep-ex/0607010] [INSPIRE].

[42] BOREXINO collaboration, *Experimental evidence of neutrinos produced in the CNO fusion cycle in the Sun*, *Nature* **587** (2020) 577 [arXiv:2006.15115] [INSPIRE].

[43] SUPER-KAMIOKANDE collaboration, *Solar neutrino measurements in Super-Kamiokande-I*, *Phys. Rev. D* **73** (2006) 112001 [hep-ex/0508053] [INSPIRE].

[44] BOREXINO collaboration, *Measurement of the solar 8B neutrino rate with a liquid scintillator target and 3 MeV energy threshold in the Borexino detector*, *Phys. Rev. D* **82** (2010) 033006 [arXiv:0808.2868] [INSPIRE].

[45] SNO collaboration, *Low energy threshold analysis of the phase I and phase II data sets of the sudbury neutrino observatory*, *Phys. Rev. C* **81** (2010) 055504 [arXiv:0910.2984] [INSPIRE].

[46] J.L. Newstead, R.F. Lang and L.E. Strigari, *Atmospheric neutrinos in next-generation xenon and argon dark matter experiments*, *Phys. Rev. D* **104** (2021) 115022 [arXiv:2002.08566] [INSPIRE].

[47] D. Baxter et al., *Recommended conventions for reporting results from direct dark matter searches*, *Eur. Phys. J. C* **81** (2021) 907 [arXiv:2105.00599] [INSPIRE].

[48] D.Z. Freedman, *Coherent neutrino nucleus scattering as a probe of the weak neutral current*, *Phys. Rev. D* **9** (1974) 1389 [INSPIRE].

[49] D.Z. Freedman, D.N. Schramm and D.L. Tubbs, *The weak neutral current and its effects in stellar collapse*, *Ann. Rev. Nucl. Part. Sci.* **27** (1977) 167 [INSPIRE].

[50] K.S. Kumar, S. Mantry, W.J. Marciano and P.A. Souder, *Low energy measurements of the weak mixing angle*, *Ann. Rev. Nucl. Part. Sci.* **63** (2013) 237 [arXiv:1302.6263] [INSPIRE].

[51] R.H. Helm, *Inelastic and elastic scattering of 187-Mev electrons from selected even-even nuclei*, *Phys. Rev.* **104** (1956) 1466 [INSPIRE].

[52] D. Aristizabal Sierra, B. Dutta, D. Kim, D. Snowden-Ifft and L.E. Strigari, *Coherent elastic neutrino-nucleus scattering with the νBDX-DRIFT directional detector at next generation neutrino facilities*, *Phys. Rev. D* **104** (2021) 033004 [arXiv:2103.10857] [INSPIRE].

[53] D. Aristizabal Sierra, *Uncertainties in the extraction of neutron density distributions*, in preparation.

[54] R. Sahu, D.K. Papoulias, V.K.B. Kota and T.S. Kosmas, *Elastic and inelastic scattering of neutrinos and weakly interacting massive particles on nuclei*, *Phys. Rev. C* **102** (2020) 035501 [arXiv:2004.04055] [INSPIRE].

[55] J.D. Lewin and P.F. Smith, *Review of mathematics, numerical factors, and corrections for dark matter experiments based on elastic nuclear recoil*, *Astropart. Phys.* **6** (1996) 87 [INSPIRE].

[56] A.K. Drukier, K. Freese and D.N. Spergel, *Detecting cold dark matter candidates*, *Phys. Rev. D* **33** (1986) 3495 [INSPIRE].

[57] K. Freese, J.A. Frieman and A. Gould, *Signal modulation in cold dark matter detection*, *Phys. Rev. D* **37** (1988) 3388 [INSPIRE].

[58] K. Freese, M. Lisanti and C. Savage, *Colloquium: annual modulation of dark matter*, *Rev. Mod. Phys.* **85** (2013) 1561 [arXiv:1209.3339] [INSPIRE].

[59] G. Cowan, K. Cranmer, E. Gross and O. Vitells, *Asymptotic formulae for likelihood-based tests of new physics*, *Eur. Phys. J. C* **71** (2011) 1554 [*Erratum ibid.* **73** (2013) 2501] [arXiv:1007.1727] [INSPIRE].

[60] C.A.J. O'Hare, A.M. Green, J. Billard, E. Figueroa-Feliciano and L.E. Strigari, *Readout strategies for directional dark matter detection beyond the neutrino background*, *Phys. Rev. D* **92** (2015) 063518 [arXiv:1505.08061] [INSPIRE].

[61] C.A.J. O'Hare, *Can we overcome the neutrino floor at high masses?*, *Phys. Rev. D* **102** (2020) 063024 [arXiv:2002.07499] [INSPIRE].

[62] DARKSIDE-20K collaboration, *DarkSide-20k: a 20 tonne two-phase LAr TPC for direct dark matter detection at LNGS*, *Eur. Phys. J. Plus* **133** (2018) 131 [arXiv:1707.08145] [INSPIRE].

[63] J. Billard et al., *Direct detection of dark matter – APPEC committee report*, arXiv:2104.07634 [INSPIRE].

[64] S. Abrahamyan et al., *Measurement of the neutron radius of 208Pb through parity-violation in electron scattering*, *Phys. Rev. Lett.* **108** (2012) 112502 [arXiv:1201.2568] [INSPIRE].

[65] HAPPEX AND PREX collaborations, *New measurements of the transverse beam asymmetry for elastic electron scattering from selected nuclei*, *Phys. Rev. Lett.* **109** (2012) 192501 [arXiv:1208.6164] [INSPIRE].

[66] M. Cadeddu, C. Giunti, Y.F. Li and Y.Y. Zhang, *Average CsI neutron density distribution from COHERENT data*, *Phys. Rev. Lett.* **120** (2018) 072501 [arXiv:1710.02730] [INSPIRE].

[67] M. Cadeddu et al., *New insights into nuclear physics and weak mixing angle using electroweak probes*, *Phys. Rev. C* **104** (2021) 065502 [arXiv:2102.06153] [INSPIRE].

[68] J.A. Formaggio and G.P. Zeller, *From eV to EeV: neutrino cross sections across energy scales*, *Rev. Mod. Phys.* **84** (2012) 1307 [arXiv:1305.7513] [INSPIRE].

[69] P. Coloma, I. Esteban, M.C. Gonzalez-Garcia and J. Menendez, *Determining the nuclear neutron distribution from coherent elastic neutrino-nucleus scattering: current results and future prospects*, *JHEP* **08** (2020) 030 [arXiv:2006.08624] [INSPIRE].

[70] J.I. Collar, A.R.L. Kavner and C.M. Lewis, *Response of CsI[Na] to Nuclear Recoils: Impact on Coherent Elastic Neutrino-Nucleus Scattering (CEνNS)*, *Phys. Rev. D* **100** (2019) 033003 [arXiv:1907.04828] [INSPIRE].

[71] J. Piekarewicz, A.R. Linero, P. Giuliani and E. Chicken, *Power of two: assessing the impact of a second measurement of the weak-charge form factor of ^{208}Pb*, *Phys. Rev. C* **94** (2016) 034316 [arXiv:1604.07799] [INSPIRE].

[72] S. Klein and J. Nystrand, *Exclusive vector meson production in relativistic heavy ion collisions*, *Phys. Rev. C* **60** (1999) 014903 [hep-ph/9902259] [INSPIRE].

[73] I. Angeli and K.P. Marinova, *Table of experimental nuclear ground state charge radii: An update*, *Atom. Data Nucl. Data Tabl.* **99** (2013) 69 [INSPIRE].

[74] PARTICLE DATA GROUP collaboration, *Review of particle physics*, *Phys. Rev. D* **98** (2018) 030001 [INSPIRE].

[75] NUTEV collaboration, *A precise determination of electroweak parameters in neutrino nucleon scattering*, *Phys. Rev. Lett.* **88** (2002) 091802 [*Erratum ibid.* **90** (2003) 239902] [hep-ex/0110059] [INSPIRE].

[76] PVDIS collaboration, *Measurement of parity violation in electron–quark scattering*, *Nature* **506** (2014) 67 [INSPIRE].

[77] SLAC E158 collaboration, *Precision measurement of the weak mixing angle in Moller scattering*, *Phys. Rev. Lett.* **95** (2005) 081601 [hep-ex/0504049] [INSPIRE].

[78] QWEAK collaboration, *Precision measurement of the weak charge of the proton*, *Nature* **557** (2018) 207 [arXiv:1905.08283] [INSPIRE].

[79] C. Wood, S. Bennett, D. Cho, B. Masterson, J. Roberts, C. Tanner and C.E. Wieman, *Measurement of parity nonconservation and an anapole moment in cesium*, *Science* **275** (1997) 1759.

[80] J. Erler and M.J. Ramsey-Musolf, *The weak mixing angle at low energies*, *Phys. Rev. D* **72** (2005) 073003 [hep-ph/0409169] [INSPIRE].

[81] DARKSIDE collaboration, *Low-mass dark matter search with the DarkSide-50 Experiment*, *Phys. Rev. Lett.* **121** (2018) 081307 [arXiv:1802.06994] [INSPIRE].

[82] J. Wyenberg and I.M. Shoemaker, *Mapping the neutrino floor for direct detection experiments based on dark matter-electron scattering*, *Phys. Rev. D* **97** (2018) 115026 [arXiv:1803.08146] [inSPIRE].

[83] A. Gaspert, P. Giampa and D.E. Morrissey, *Neutrino backgrounds in future liquid noble element dark matter direct detection experiments*, arXiv:2108.03248 [inSPIRE].

[84] CONUS collaboration, *Constraints on elastic neutrino nucleus scattering in the fully coherent regime from the CONUS experiment*, *Phys. Rev. Lett.* **126** (2021) 041804 [arXiv:2011.00210] [inSPIRE].

[85] CONNIE collaboration, *Exploring low-energy neutrino physics with the coherent neutrino nucleus interaction experiment*, *Phys. Rev. D* **100** (2019) 092005 [arXiv:1906.02200] [inSPIRE].

[86] R. Strauss et al., *The ν-cleus experiment: A gram-scale fiducial-volume cryogenic detector for the first detection of coherent neutrino-nucleus scattering*, *Eur. Phys. J. C* **77** (2017) 506 [arXiv:1704.04320] [inSPIRE].

[87] SBC, CEνNS THEORY GROUP AT IF-UNAM collaboration, *Physics reach of a low threshold scintillating argon bubble chamber in coherent elastic neutrino-nucleus scattering reactor experiments*, *Phys. Rev. D* **103** (2021) L091301 [arXiv:2101.08785] [inSPIRE].

[88] J. Liao and D. Marfatia, *COHERENT constraints on nonstandard neutrino interactions*, *Phys. Lett. B* **775** (2017) 54 [arXiv:1708.04255] [inSPIRE].

[89] D. Aristizabal Sierra, V. De Romeri and N. Rojas, *CP violating effects in coherent elastic neutrino-nucleus scattering processes*, *JHEP* **09** (2019) 069 [arXiv:1906.01156] [inSPIRE].

[90] M. Abdullah, D. Aristizabal Sierra, B. Dutta and L.E. Strigari, *Coherent elastic neutrino-nucleus scattering with directional detectors*, *Phys. Rev. D* **102** (2020) 015009 [arXiv:2003.11510] [inSPIRE].

[91] J.A. Grifols and E. Masso, *Constraints on finite range baryonic and leptonic forces from stellar evolution*, *Phys. Lett. B* **173** (1986) 237 [inSPIRE].

[92] J.A. Grifols, E. Masso and S. Peris, *Energy loss from the sun and RED giants: bounds on short range baryonic and leptonic forces*, *Mod. Phys. Lett. A* **4** (1989) 311 [inSPIRE].

[93] J.H. Chang, R. Essig and S.D. McDermott, *Revisiting supernova 1987A constraints on dark photons*, *JHEP* **01** (2017) 107 [arXiv:1611.03864] [inSPIRE].

[94] A.G. Beda et al., *Upper limit on the neutrino magnetic moment from three years of data from the GEMMA spectrometer*, arXiv:1005.2736 [inSPIRE].

[95] Y. Farzan, M. Lindner, W. Rodejohann and X.-J. Xu, *Probing neutrino coupling to a light scalar with coherent neutrino scattering*, *JHEP* **05** (2018) 066 [arXiv:1802.05171] [inSPIRE].

[96] D. Aristizabal Sierra, V. De Romeri and N. Rojas, *COHERENT analysis of neutrino generalized interactions*, *Phys. Rev. D* **98** (2018) 075018 [arXiv:1806.07424] [inSPIRE].

[97] V. Brdar, W. Rodejohann and X.-J. Xu, *Producing a new fermion in coherent elastic neutrino-nucleus scattering: from neutrino mass to dark matter*, *JHEP* **12** (2018) 024 [arXiv:1810.03626] [inSPIRE].

[98] D.G. Cerdeño, M. Fairbairn, T. Jubb, P.A.N. Machado, A.C. Vincent and C. Bœhm, *Physics from solar neutrinos in dark matter direct detection experiments*, *JHEP* **05** (2016) 118 [*Erratum ibid.* **09** (2016) 048] [arXiv:1604.01025] [inSPIRE].

[99] M. Hoferichter, J. Ruiz de Elvira, B. Kubis and U.-G. Meißner, *High-precision determination of the pion-nucleon σ term from Roy-Steiner equations*, *Phys. Rev. Lett.* **115** (2015) 092301 [arXiv:1506.04142] [inSPIRE].

[100] J. Ellis, N. Nagata and K.A. Olive, *Uncertainties in WIMP dark matter scattering revisited*, *Eur. Phys. J. C* **78** (2018) 569 [arXiv:1805.09795] [INSPIRE].

[101] D.K. Papoulias, *COHERENT constraints after the COHERENT-2020 quenching factor measurement*, *Phys. Rev. D* **102** (2020) 113004 [arXiv:1907.11644] [INSPIRE].

[102] O.G. Miranda, D.K. Papoulias, M. Tórtola and J.W.F. Valle, *Probing neutrino transition magnetic moments with coherent elastic neutrino-nucleus scattering*, *JHEP* **07** (2019) 103 [arXiv:1905.03750] [INSPIRE].

[103] D.K. Papoulias, T.S. Kosmas and Y. Kuno, *Recent probes of standard and non-standard neutrino physics with nuclei*, *Front. in Phys.* **7** (2019) 191 [arXiv:1911.00916] [INSPIRE].

[104] D.K. Papoulias and T.S. Kosmas, *COHERENT constraints to conventional and exotic neutrino physics*, *Phys. Rev. D* **97** (2018) 033003 [arXiv:1711.09773] [INSPIRE].

[105] D. Aristizabal Sierra, R. Branada, O.G. Miranda and G. Sanchez Garcia, *Sensitivity of direct detection experiments to neutrino magnetic dipole moments*, *JHEP* **12** (2020) 178 [arXiv:2008.05080] [INSPIRE].

[106] C. Giunti and A. Studenikin, *Neutrino electromagnetic interactions: a window to new physics*, *Rev. Mod. Phys.* **87** (2015) 531 [arXiv:1403.6344] [INSPIRE].

[107] P. Vogel and J. Engel, *Neutrino electromagnetic form-factors*, *Phys. Rev. D* **39** (1989) 3378 [INSPIRE].

[108] BOREXINO collaboration, *Limiting neutrino magnetic moments with Borexino Phase-II solar neutrino data*, *Phys. Rev. D* **96** (2017) 091103 [arXiv:1707.09355] [INSPIRE].

[109] TEXONO collaboration, *Measurement of Nu(e)-bar -Electron Scattering Cross-Section with a CsI(Tl) Scintillating Crystal Array at the Kuo-Sheng Nuclear Power Reactor*, *Phys. Rev. D* **81** (2010) 072001 [arXiv:0911.1597] [INSPIRE].

[110] XENON collaboration, *Excess electronic recoil events in XENON1T*, *Phys. Rev. D* **102** (2020) 072004 [arXiv:2006.09721] [INSPIRE].

[111] COHERENT collaboration, *COHERENT Collaboration data release from the first observation of coherent elastic neutrino-nucleus scattering*, arXiv:1804.09459 [INSPIRE].

[112] COHERENT collaboration, *COHERENT Collaboration data release from the first detection of coherent elastic neutrino-nucleus scattering on argon*, arXiv:2006.12659 [INSPIRE].

[113] J.C. Zettlemoyer, *First detection of coherent elastic neutrino-nucleus scattering on an argon target*, Ph.D. Thesis, Indiana University, Bloomington (main) (2020) [INSPIRE].

[114] M. Cadeddu, F. Dordei, C. Giunti, Y.F. Li, E. Picciau and Y.Y. Zhang, *Physics results from the first COHERENT observation of coherent elastic neutrino-nucleus scattering in argon and their combination with cesium-iodide data*, *Phys. Rev. D* **102** (2020) 015030 [arXiv:2005.01645] [INSPIRE].